1   **Supplementary Information**

2   Carbon oxidation with sacrificial anodes to inhibit O_2 evolution in membrane-

3   less bioelectrochemical systems for microbial electrosynthesis

4   *Nils Rohbohm[a], Tianran Sun[a,b], Ramiro Blasco-Gómez[a,c], James M. Byrne[d,e],,*

5   *Andreas Kappler[d,f] and Largus T. Angenent*[a,f,g,h,i]*

6   [a]Environmental Biotechnology Group, Department of Geosciences, University of Tübingen, Schnarrenbergstr. 94-96, 72076
7   Tübingen, Germany

8   [b]State Key Lab of Urban and Regional Ecology, Research Center for Eco-Environmental Sciences, Chinese Academy of Sciences,
9   Beijing 100085, China

10   [c]Laboratory of Chemical and Environmental Engineering (LEQUiA), Institute of the Environment, University of Girona, Carrer Maria
11   Aurelia Capmany, 69, 17003 Girona, Spain

12   [d] Geomicrobiology group, Department of Geosciences, University of Tübingen, Schnarrenbergstr. 94-96, 72076 Tübingen,
13   Germany

14   [e] School of Earth Sciences, University of Bristol, Wills Memorial Building, Queens Road, Bristol, BS8 1RJ, United Kingdom

15   [f]Cluster of Excellence: EXC 2124: Controlling Microbes to Fight Infection, Tübingen, 72076, Germany

16   [g] AG Angenent, Max Planck Institute for Biology, Max Planck Ring 5, D-72076 Tübingen, Germany

17   [h] Department of Biological and Chemical Engineering, Aarhus University, Gustav Wieds Vej 10D, 8000 Aarhus C, Denmark

18   [i] The Novo Nordisk Foundation CO_2 Research Center (CORC), Aarhus University, Gustav Wieds Vej 10C, 8000 Aarhus C, Denmark

19

20   **Supplementary note 1:**

21   **Determination of the exchange current density and Tafel slope**

22   For the determination of the exchange current density for the carbon oxidation, OER, and HER, the Butler-Volmer equation (**Eq.**

23   **S1**) was used and transformed to determine j_0 from its interception at the y-axis.[1] The Butler-Volmer equation (**Eq. S1**) is described

24   as followed:

$$j = j_0 \left\{ exp \left[\frac{\alpha_a zF}{RT} \eta \right] - exp \left[\frac{\alpha_c zF}{RT} \eta \right] \right\}$$

(S1)

25   With j the current density, j_0 the exchange current density, α_a and α_c the anodic and cathodic charge transfer coefficient,

26   respectively, z the number of electrons involved in the reaction, F the Faraday constant, R the universal gas constant, T the

27   temperature, and η the activation overpotential.

28   When η>>0, the **Eq. S1** simplifies to **Eq. S2** :

$$\eta = \frac{2.3\, RT}{\alpha F} log j_0 - \frac{2.3\, RT}{\alpha F} log j$$

(S2)

29   **Eq. S2** can be transformed into the Tafel equation to calculate the Tafel slope, which was used to calculate the Tafel slopes of

30   magnetite:

$$\eta = \pm \frac{2.3\, RT}{\alpha F} log \frac{j}{j_0} + A$$

(S3)

$$\eta = B log \frac{j}{j_0} + A$$

(S4)

31   With B the Tafel slope, and A the symmetry factor. The exchange current density j_0 and the Tafel slope are calculated from

32      $log|j|$ *vs.* η by the interception of the y-axis and the slope, respectively.

33

34 **Supplementary note 2:**

35 **Magnetite analyses**

36 We investigated magnetite as a possible redox mediator. We fabricated magnetite anodes with activated carbon, which is our

37 carbon source for carbon oxidation, to increase the conductivity of magnetite, which is a semi-conductor.[2] Since the conductivity

38 of the electrode can vary depending on the amount of activated carbon used, we investigated which ratio of magnetite to

39 activated carbon is suitable for higher current generation, longevity, and inhibition of O_2 evolution. Therefore, we performed

40 abiotic tests with different ratios of magnetite and activated carbon ranging from 20% to 100% of the total activated carbon. We

41 used the chronoamperometric method to determine the electronic conductivity of our mixtures and set the WE at +0.6 V *vs*.

42 Ag/AgCl. The current of a chronoamperometric graph decreased exponentially to reach an asymptotic value, which was used to

43 calculate the conductivity (**Fig. S11**). The specific electronic conductivity σ was calculated (**Eq. S5**).

$$\sigma = \frac{I \cdot D}{E \cdot A} \tag{S5}$$

44 Where I is the asymptotic current, D is the thickness of the electrode (D = 0.4 cm), E is the applied potential, and A is the surface

45 area of the electrode (A = 0.28 cm^2). The calculated specific electronic conductivities of 40% magnetite and 60% activated carbon

46 showed the highest electronic conductivity with 3.89×10^{-4} S·cm^{-1} and was further analyzed for its ability to inhibit O_2 (**Table S2**).

47 A critical aspect of sufficient electrical conductivity is a homogenous distribution of magnetite on activated carbon particles.

48 Ideally, only a thin layer of magnetite is adsorbed on the surface of the activated carbon. To analyze the distribution of magnetite

49 on activated carbon, we characterized synthesized magnetite on activated carbon with X-ray diffraction (XRD). We compared

50 synthesized magnetite with the following materials: **(1)** pure magnetite; **(2)** pure activated carbon; and **(3)** commercial magnetite

51 (**Fig. S12**). The XRD patterns of magnetite, magnetite on activated carbon, and commercial magnetite show overlapping

52 diffraction peaks for the whole spectrum, confirming that our synthesis contains magnetite. Further comparison of the XRD peaks

53 shows a good agreement with standard patterns, indicating high crystalline quality. However, because maghemite's XRD pattern

54 is virtually indistinguishable from the XRD pattern of magnetite, we analyzed the Fe(II)/Fe(III) ratio with the ferrozine assay. The

55 ratio of Fe(II)/Fe(III) found in our samples corresponded to 0.40 ± 0.1, which is 20% lower than the ideal ratio of 0.5 for magnetite.

56 This means that 20% of our material was oxidized, likely to maghemite. The XRD pattern of the activated carbon can be attributed

57 to amorphous carbon that is also observed in magnetite coated activated carbon.

Scanning electron micrograph of magnetite on activated carbon demonstrated a rough and porous particle (**Fig. S13A**). Furthermore, close-up views of the particle showed that magnetite was synthesized as round-shaped nanoparticles (**Fig. S13B,C**). However, it was not possible to identify whether magnetite was homogeneously coated on activated carbon. To underline the homogenous distribution of magnetite, we performed EDX to detect the iron on the surface. By detecting the Fe with Fe Kα energy-dispersive X-ray spectroscopy (EDX) elemental mapping of magnetite-coated activated carbon, we detected the distribution of Fe. The overlay of a magnetite-coated activated carbon particle SEM micrograph with the elemental mapping of Fe confirmed that Fe was very well dispersed on top of the activated carbon particle (**Fig. S14** and **S15**).

The stability of magnetite anodes is primarily determined by the crystal structure and purity of the magnetite mineral

We calculated the conductivity of different magnetite to activated carbon ratios and found that the ratio of 40%:60% magnetite to activated carbon obtained higher conductivities for our electrodes (**Eq. 5** and **Fig. S11**). To understand how this ratio functions in stability and longevity, we prepared triplicates of 40%:60% magnetite to activated carbon electrodes as our counter electrodes and poised the carbon cloth WE at -0.8 V *vs.* Ag/AgCl. After 7 days, the liquid/electrode interface developed an orange precipitate of Fe(III) at each electrode. After the experiment, we analyzed each Fe(II)/Fe(III) electrode ratio with a sequential extraction. We compared them with the starting material (**Fig. S16**) and analyzed the abundance of Fe(II) and Fe(III) for each section (electrode liquid interface, middle section, upper section). Here, the starting material was partially oxidized with a stoichiometric ratio of around 0.44. After 7 days of oxidation, the outer layer of the magnetite particle was nearly completed oxidized, while the stoichiometric ratio of the bulk was similar to the initial stoichiometric ratio of magnetite. In conclusion, activated carbon coated magnetite showed nearly complete oxidation at the outer layer that might prevent a stable and durable anode. Refer to the main text for further informations on the durability of magnetite anodes under section "Magnetite, which is an alternative redox mediator to soluble iron, shortened the optimum performance period"

Table S1 | Comparison of abiotic and biotic current densities with their respective coulombic efficiencies and references

Product	Current density [mA cm^{-2}]	Coulombic Efficiency [%]
Abiotic		
H_2	Up to 2000	99 [3]
Ethanol	250	46 [4]
CH_4	200	70 [5]
Biotic		
Acetate	10	100 [6]
CH_4	1	99 [7]

79

80

Table S2│The electronic conductivity of different activated carbon to magnetite and hematite percentages calculated by chronoamperometry (CA) method.

Activated carbon to magnetite	Electronic conductivity [S/cm]
100% activated carbon	5.08×10^{-8}
60% activated carbon, 40% magnetite	3.89×10^{-4}
40% activated carbon, 60% magnetite	2.91×10^{-4}
20% activated carbon, 80% magnetite	1.91×10^{-4}
60% activated carbon, 40% maghemite	5.31×10^{-6}

81

82

83

84
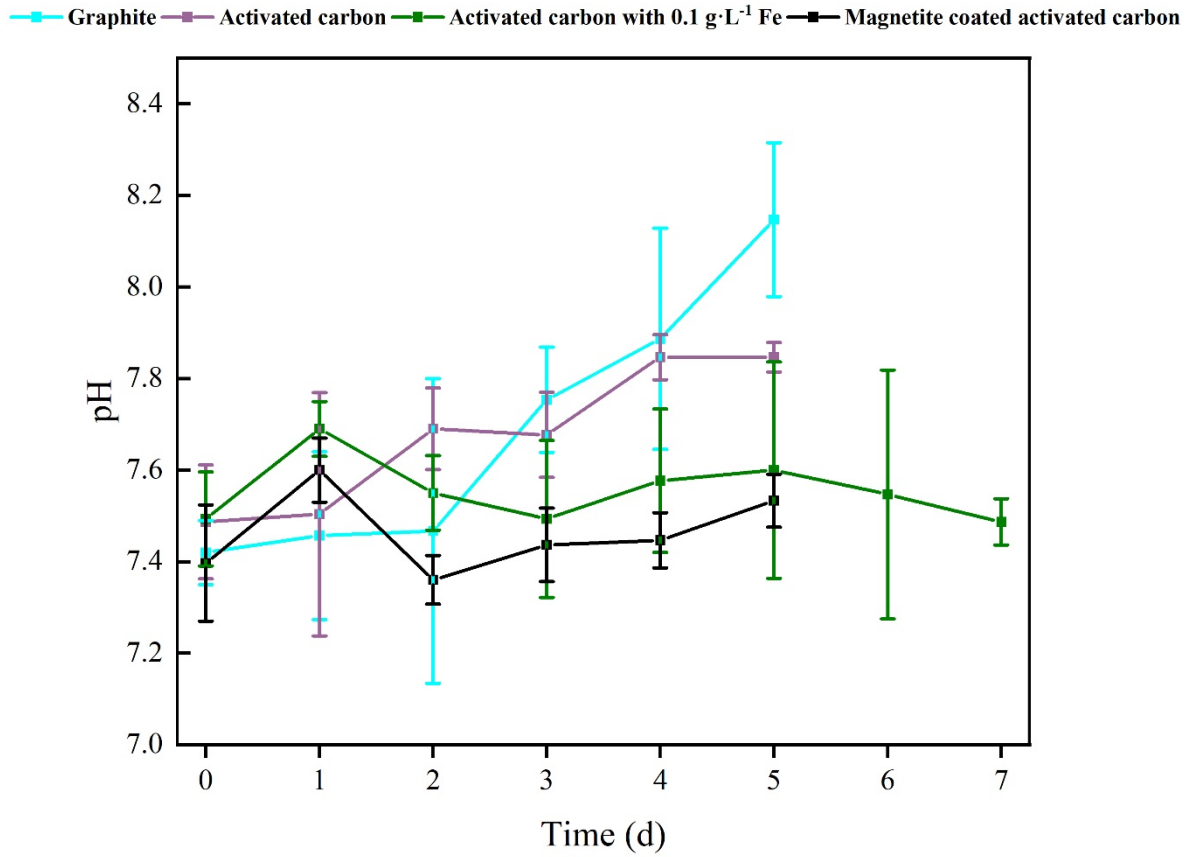
Figure S1: Measured pH during some of the BES experiments using graphite, activated carbon with and without added iron, and magnetite-coated activated-carbon anodes.

85
86
87

88
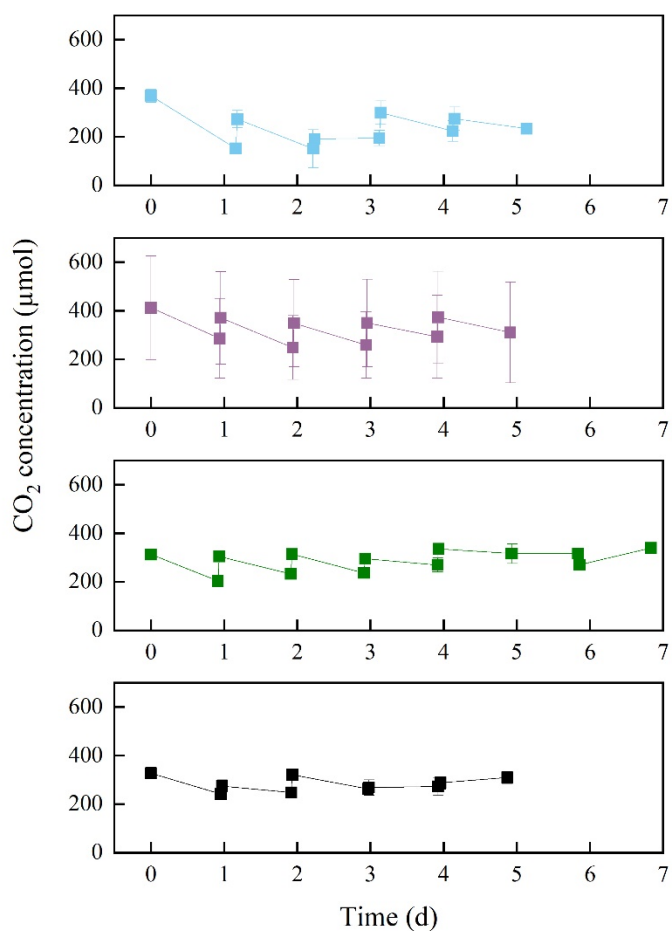
Figure S2: CO_2 concentration during batch experiments throughout time with the thermophilic archaeon *M. thermautotrophicus* ΔH. Graphite-rod and activated-carbon anodes were included with three treatments for activated carbon, including iron additions (soluble iron and magnetite). The error bars show the standard deviation for the average data from triplicate systems.
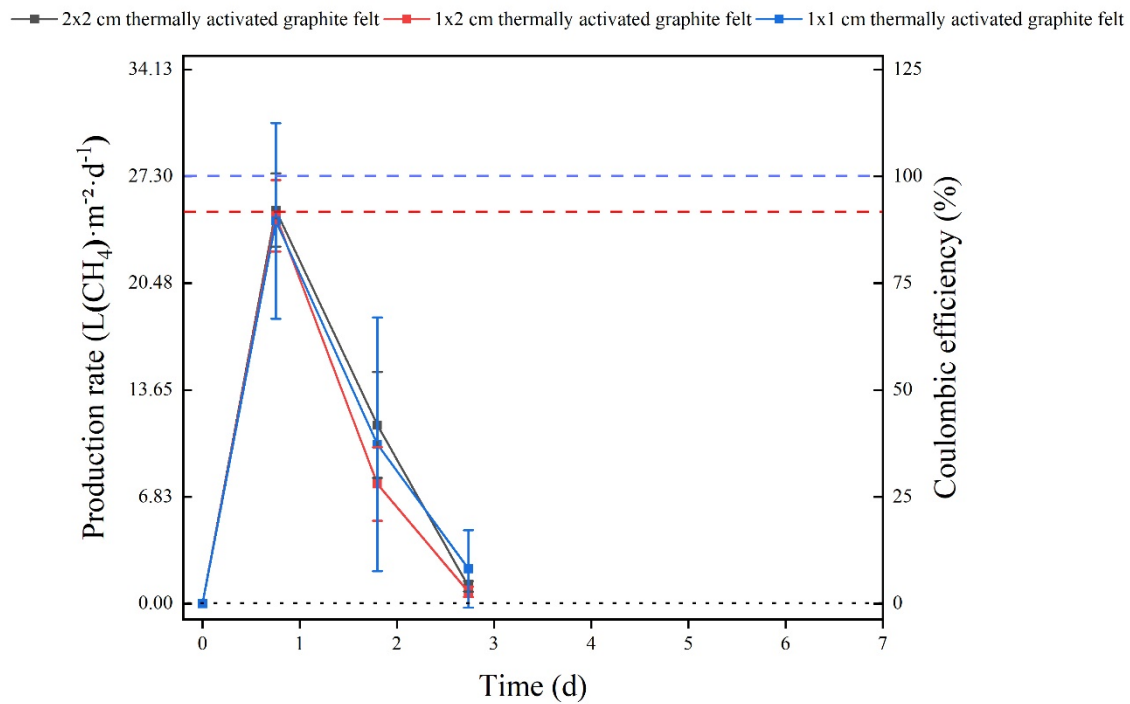
Figure S3: CH_4 production rates corrected to the cathode surface area and Coulombic efficiencies (at I = 1 A·cm^{-2}) during batch experiments in our BES throughout time with L-cysteine and with the thermophilic archaeon *M. thermautotrophicus* ΔH. Thermally activated graphite felt anodes were included with three different conditions (1x1 cm , 1x2 cm graphite felt, and 2x2 cm). The error bars show the standard deviation for the average data from triplicate systems. Carbon cloth was used as the cathode: **(**Y-axis 1) cathode-based geometric CH_4 production rates; and **(**Y-axis 2**)** Coulombic efficiencies.

103
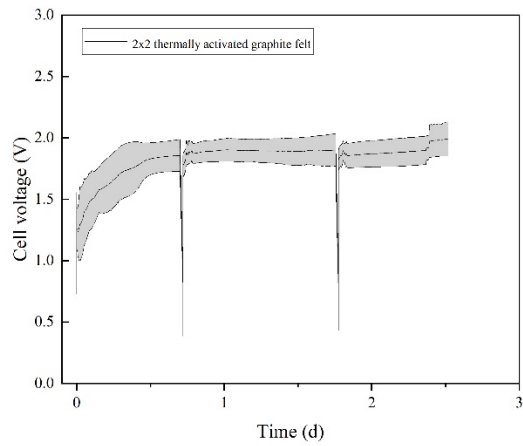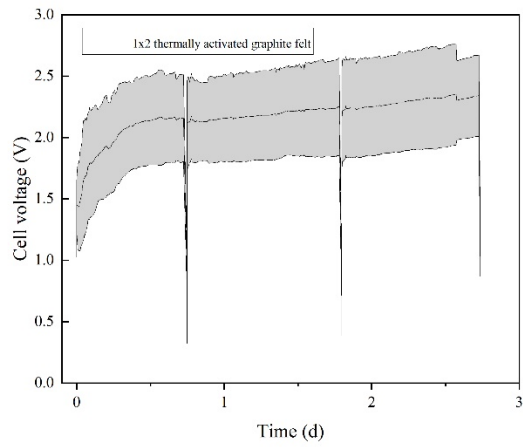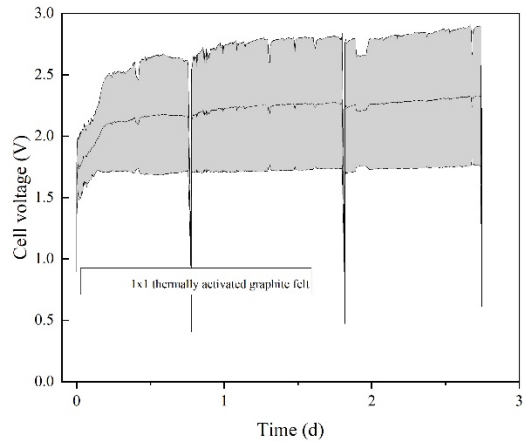
Figure S4: Cell voltages of the BES experiment performed in triplicates using three different sizes (1x1, 1x2, and 2x2 cm) of the thermally activated graphite felt as anode.

10

106
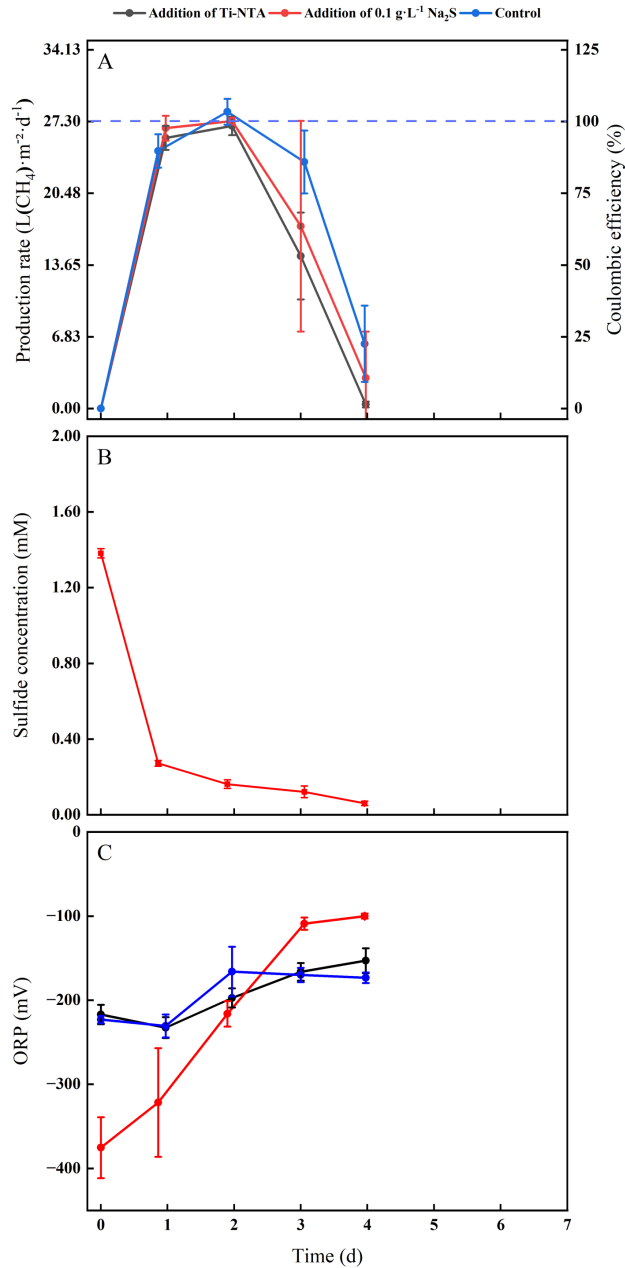
Figure S5: BES experiments with different reducing agents: (**A**) CH₄ production rates corrected to the cathode surface area and Coulombic efficiencies (at I = 1 A·cm⁻²) during batch experiments throughout time with the thermophilic archaeon *M. thermautotrophicus* ΔH. Thermally activated graphite felt anodes were included with three different conditions (addition of Ti-NTA with L-cysteine, addition of 0.1 g·L⁻¹ Na₂S without L-cysteine, and control with L-cysteine). Ti-NTA was supplied at a ratio of 1:1000 at the beginning and every sampling point. Each condition included iron additions of 0.1 g·L⁻¹. Carbon cloth was used as the cathode: (**Y**-axis 1) cathode-based geometric CH₄ production rates; and (**Y**-axis 2) Coulombic efficiencies; (**B**) Sulfide concentrations during the addition of 0.1 g·L⁻¹ Na₂S batch experiment throughout time with the thermophilic archaeon *M. thermautotrophicus* ΔH; and (**C**) ORP measurement for all three conditions throughout time with the thermophilic archaeon *M. thermautotrophicus* ΔH. The error bars show the standard deviation for the average data from triplicate systems

116

11
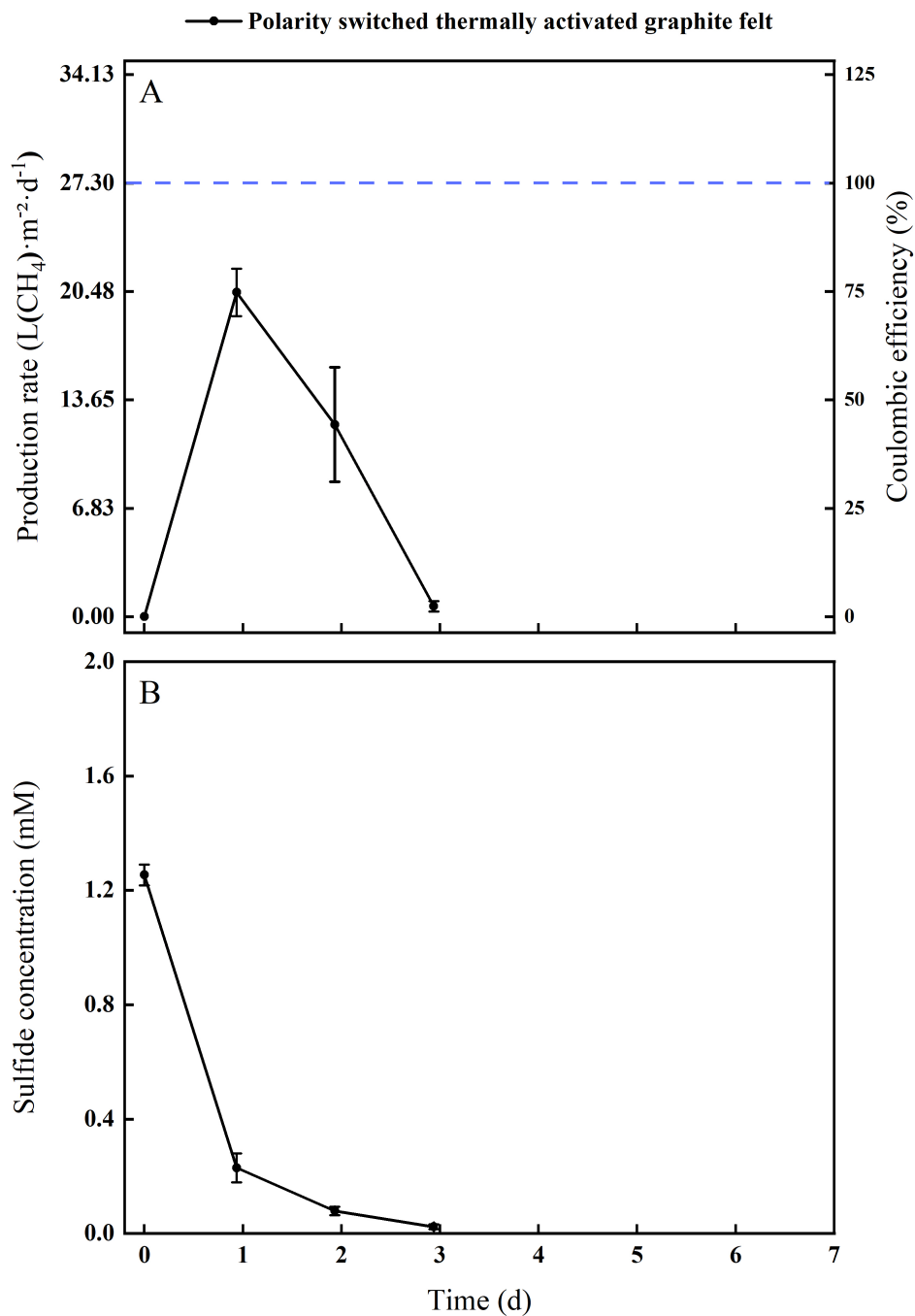
Figure S6: BES experiment with polarity switch: (**A**) CH_4 production rate corrected to the cathode surface area and Coulombic efficiency (at I = 1 A·cm⁻²) during batch experiments throughout time with the thermophilic archaeon *M. thermautotrophicus* ΔH when the polarity of the thermally activated graphite felt anodes was switched every 4h. 0.1 g·L⁻¹ Na₂S was supplied to the medium instead of L-cysteine; and (**B**) Sulfide concentrations during batch experiments throughout time. The error bars show the standard deviation for the average data from triplicate systems.

125
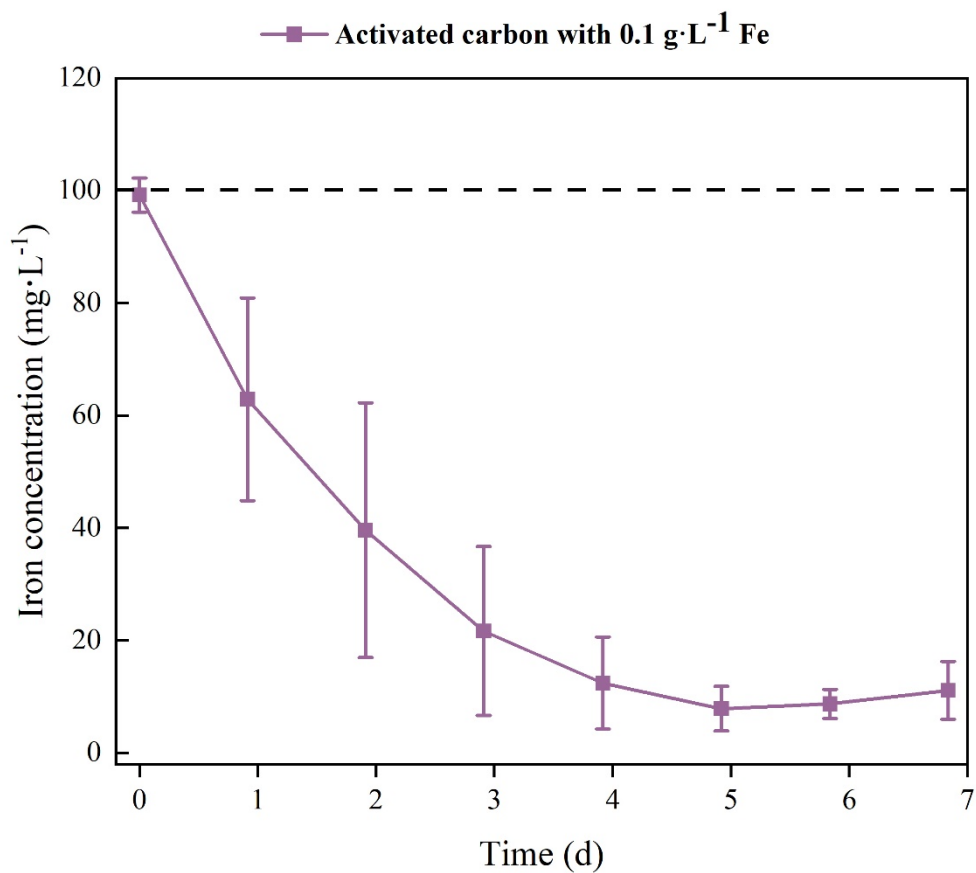
Figure S7: iron concentration during batch experiments of activated carbon-based anode with added iron throughout time with the thermophilic archaeon *M. thermautotrophicus* ΔH.
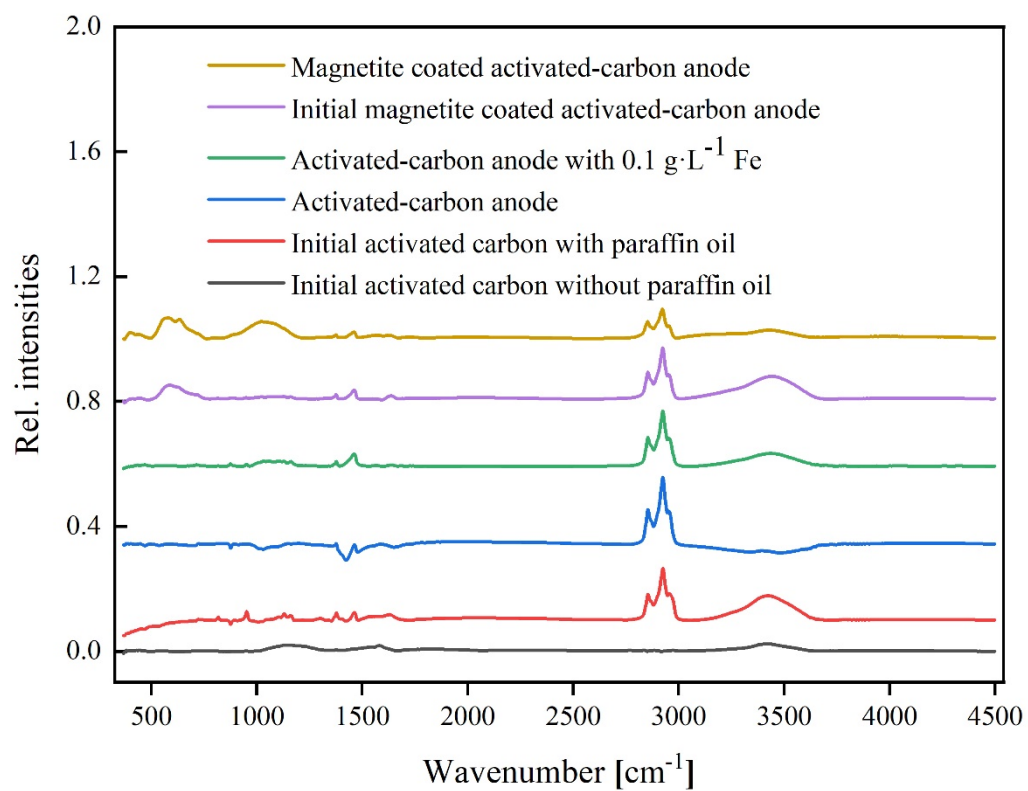
129

130

131   **Figure S8:** example of carbon corrosion after the BES experiment. The corroded carbon turned the medium black.
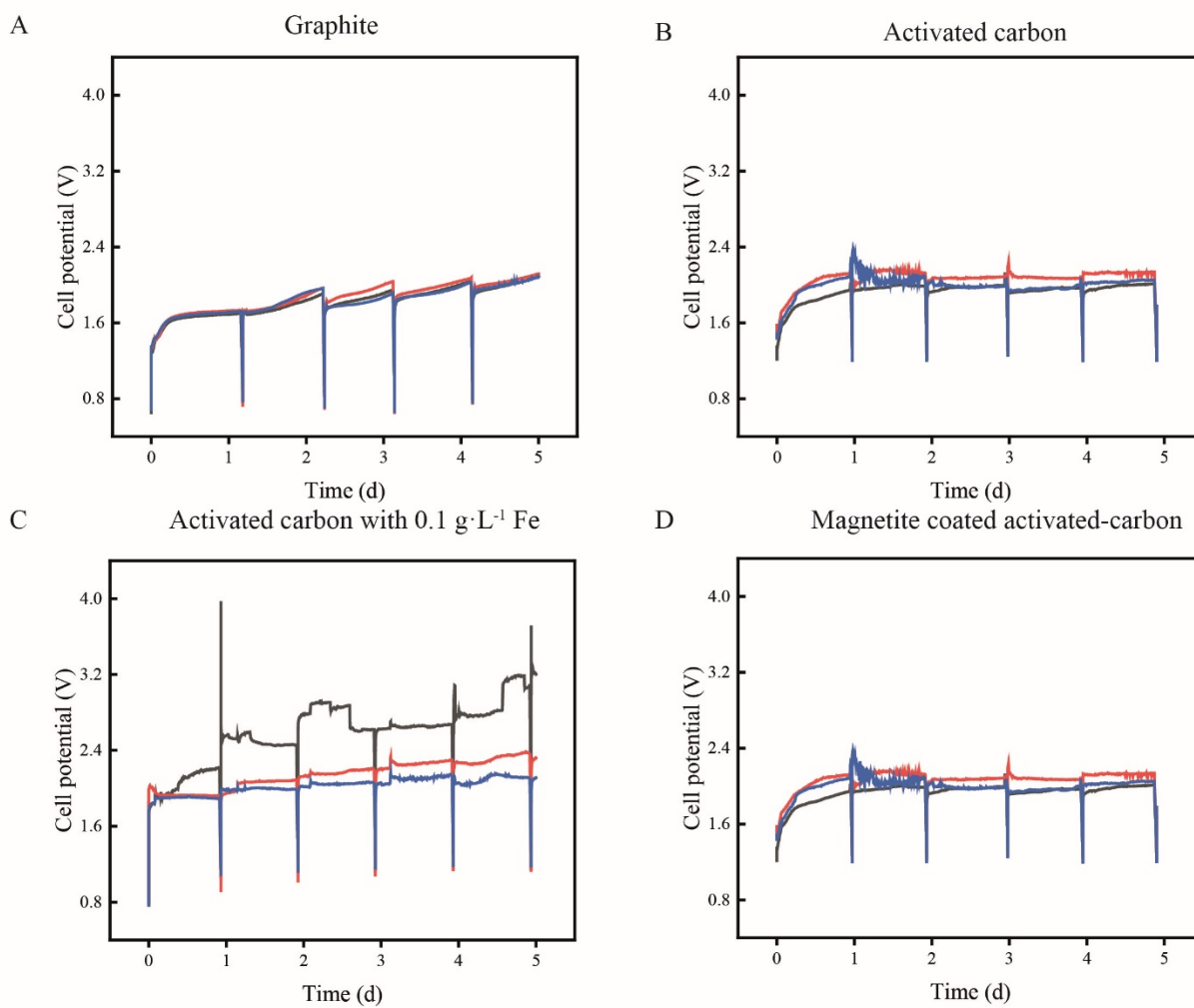
132

133

134

135 **Figure S9:** FTIR measurements of initial activated carbon with and without paraffin oil, activated-carbon
136 anode with 0.1 g·L^{-1} Fe, initial magnetite-coated activated-carbon anode, and magnetite-coated activated-carbon anode. Samples
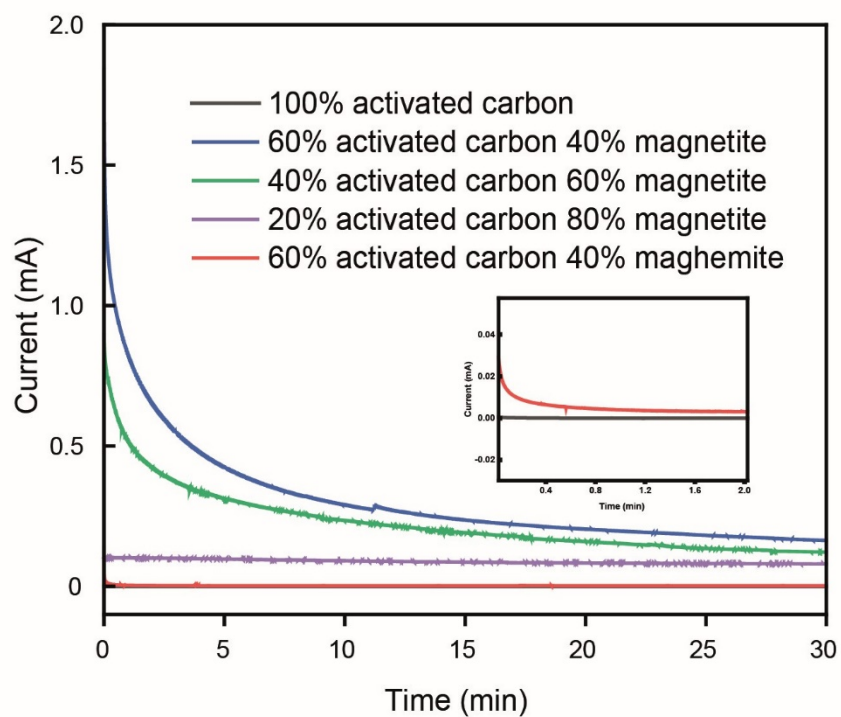137 were taken from dried anodes after 5 days of oxidation.

138

139

Figure S10: Cell potentials of the BES experiment performed in triplicates using different carbon based anodes: **(A)** graphite; **(B)** activated-carbon; **(C)** activated-carbon with 0.1 g·L^{-1} Fe; and **(D)** magnetite-coated activated-carbon.
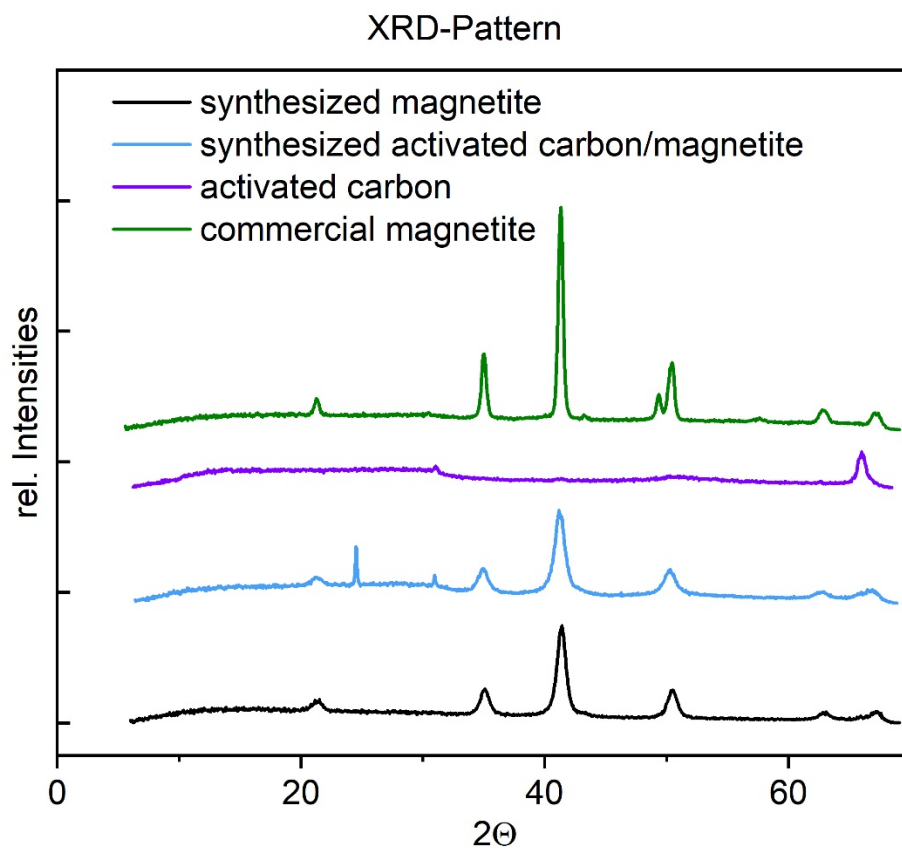
144

145

146

Figure S11: Chronoamperometic current traces of 100% activated carbon, 60% activated carbon & 40% magnetite, 40 % activated carbon & 60% magnetite, 20% activated carbon & 80% magnetite, and 60% activated carbon & 40% maghemite at +0.6 V in 66 mM phosphate buffer.

150

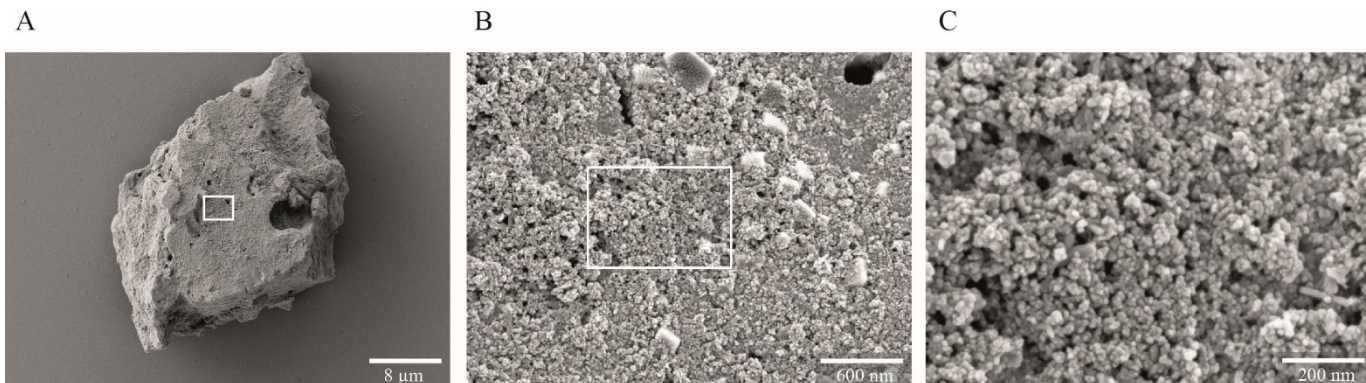**XRD-Pattern**

Legend:
— synthesized magnetite
— synthesized activated carbon/magnetite
— activated carbon
— commercial magnetite

y-axis: rel. Intensities
x-axis: 2Θ

Figure S12: XRD pattern of synthesized magnetite, synthesized magnetite coated on activated carbon, activated carbon, and commercial magnetite.

155
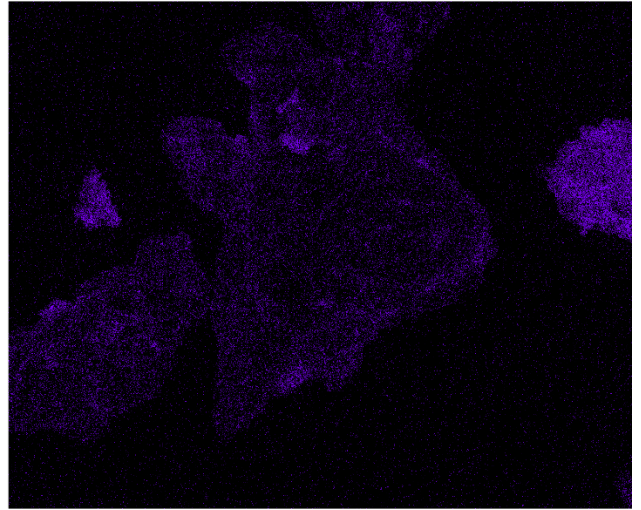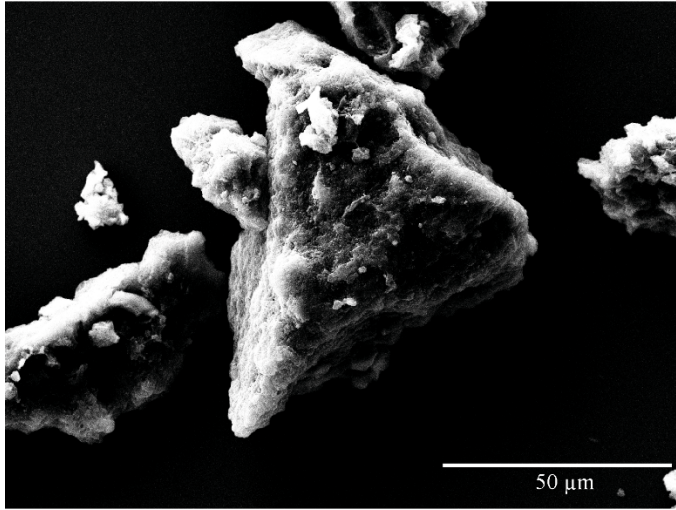
Figure S13: Scanning electron micrographs of magnetite-coated activated carbon: **(A)** Particle of magnetite-coated activated carbon with a 2300x magnification; **(B)** close-up from the rectangular-shaped area of (A) with a magnification of 35000x; and **(C)** close-up from the rectangular-shaped area of (B) with a magnification of 95000x.
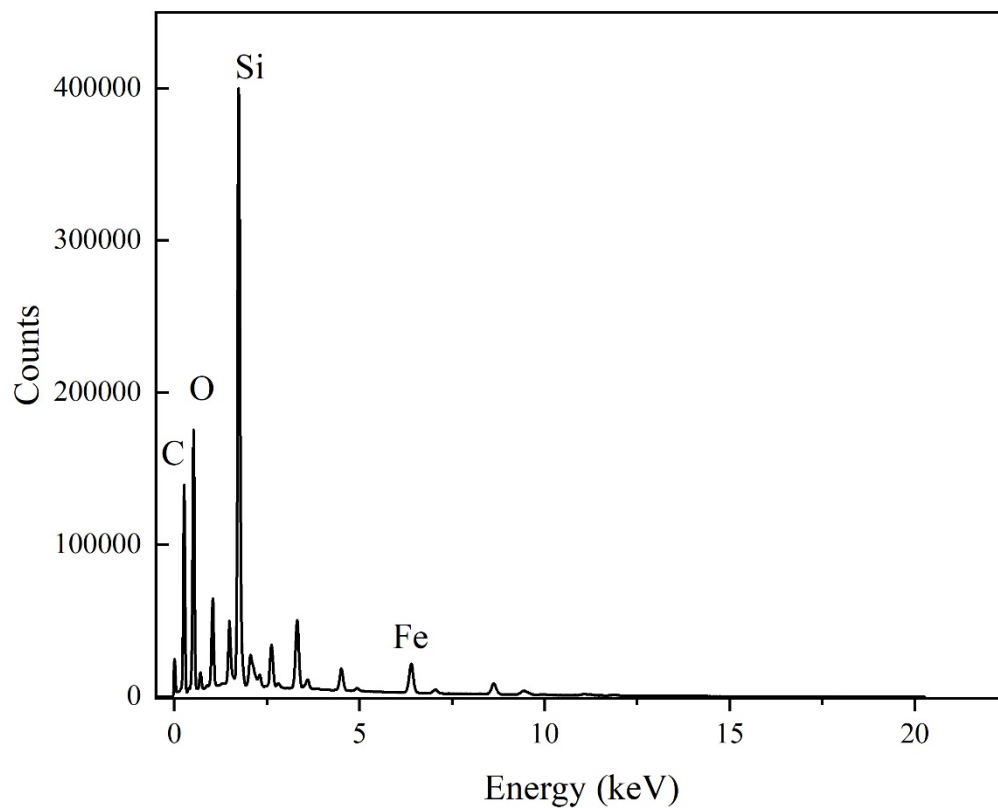
50 µm

160

161 **Figure S14:** Scanning electron micrograph and its EDX Fe Kα elemental mapping (in violet).
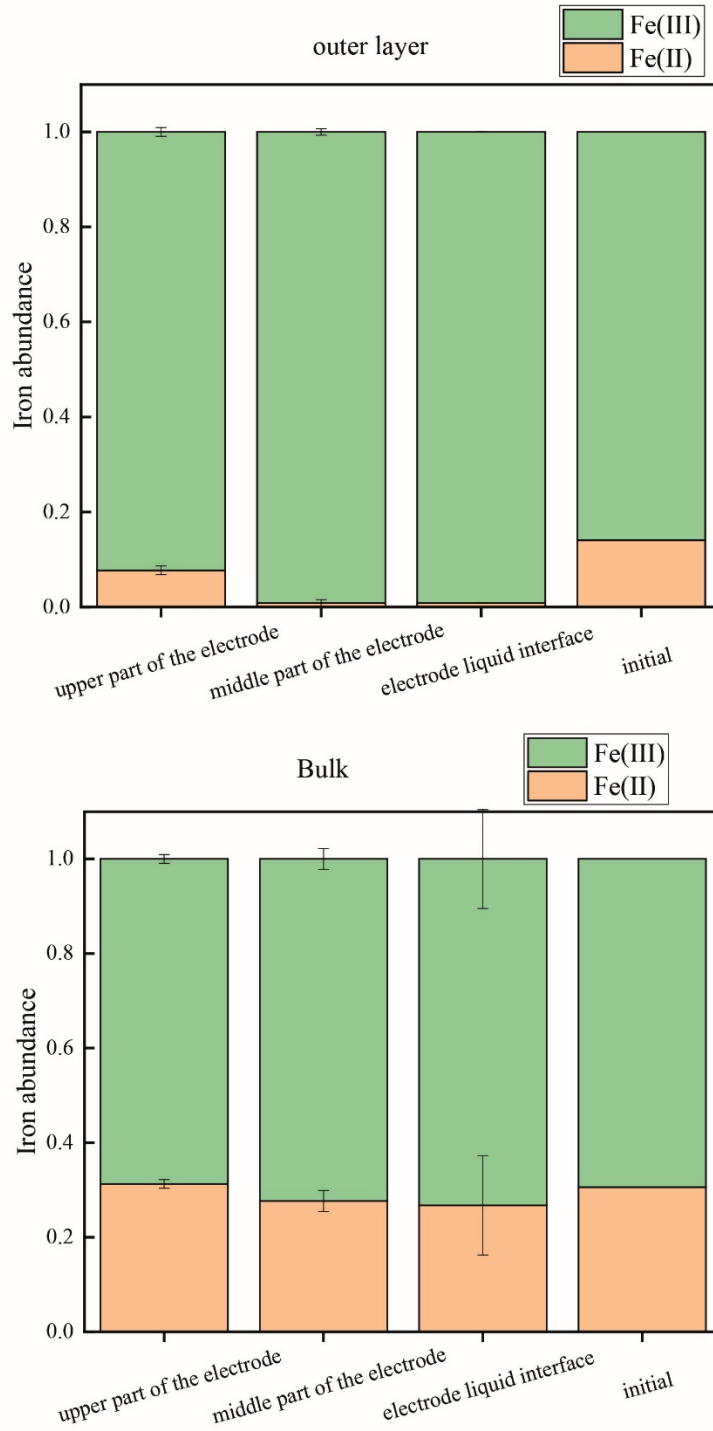
162

163

164   **Figure S15:** EDX Fe Kα elemental mapping spectrum from **Fig. S14**.

165

166

Figure S16: Oxidation state of magnetite. Measured Fe(II) and Fe(III) abundance from the outer layer and bulk from the upper part, middle part, and the electrode liquid interface.

169   **References**

170   1.   A. J. Bard and L. R. Faulkner, *Electrochemical Methods: Fundamentals and Applications,*
171   *2nd Edition*, Wiley, Hoboken, NJ, USA, 2000.
172   2.   R. M. Cornell and U. Schwertmann, *The Iron Oxides: Structure, Properties, Reactions,*
173   *Occurrence and Uses*, Wiley, Weinheim, Germany, 2003.
174   3.   H. Lee, B. Lee, M. Byun and H. Lim, *Energy Conversion and Management*, 2020, **224**,
175   113477.
176   4.   S. Ma, M. Sadakiyo, R. Luo, M. Heima, M. Yamauchi and P. J. A. Kenis, *Journal of Power*
177   *Sources*, 2016, **301**, 219-228.
178   5.   T. Zhang, W. Li, K. Huang, H. Guo, Z. Li, Y. Fang, R. M. Yadav, V. Shanov, P. M. Ajayan,
179   L. Wang, C. Lian and J. Wu, *Nature Communications*, 2021, **12**, 5265.
180   6.   L. Jourdin, T. Grieger, J. Monetti, V. Flexer, S. Freguia, Y. Lu, J. Chen, M. Romano, G.
181   G. Wallace and J. Keller, *Environmental Science & Technology*, 2015, **49**, 13566-13574.
182   7.   F. Kracke, J. S. Deutzmann, W. Gu and A. M. Spormann, *Green Chemistry*, 2020, **22**,
183   6194-6203.

184